LRP 643/99 August 1999

Recent Results in ECH and ECCD Experiments in the TCV Tokamak

M.A. Henderson, T.P. Goodman, R. Behn,
S. Coda, J-P. Hogge, Y. Martin, Y. Peysson,
Z.A. Pietrzyk, A. Pochelon, O. Sauter, M.Q. Tran,
and the TCV Team

Presented at the Fourth International Workshop on
Strong Microwaves in Plasmas
August 1-8, 1999, Nizhny Novgorod, Russia

ISSN 0458-5895

Recent Results in ECH and ECCD Experiments in the TCV Tokamak

M.A. Henderson, T.P. Goodman, R. Behn, S. Coda, J-P. Hogge, Y. Martin, Y. Peysson[1], Z.A. Pietrzyk, A. Pochelon, O. Sauter, M.Q. Tran, and the TCV Team

Centre de Recherches en Physique des Plasmas,
Ecole Polytechnique Fédérale de Lausanne
Association EURATOM-Confédération Suisse,
CH-1015 Lausanne EPFL, Switzerland

[1] CEA/Cadarache, 13108 Saint Paul-Lez-Durances Cedex, France

INTRODUCTION:

The ECH system on the tokamak TCV (Tokamak à Configuration Variable) has reached completion of the first of three stages of auxiliary heating installations with the operation of the first cluster of three 82.7GHz gyrotrons each of 0.5MW, 2.0s pulse length second harmonic X-mode (X2). The overall ECRH project is to have 3.0MW of X2 (six gyrotrons at 82.7GHz) and 1.5MW (three gyrotrons at 118GHz, capable of 210s pulse lengths but to be operated up to 2.0s at CRPP) at the third harmonic X-mode (X3).

During the past operational campaign a variety of experiments have been performed using the available ECH power of 1.5MW. Some of these include: commissioning of the launching antenna, studies of confinement as a function of plasma shape and assisted L to H-mode transitions. Also studies with non-zero toroidal launch angles have been performed including scans of toroidal injection angle with co- and counter-ECCD, up-down asymmetry associated with an inherent off-axis ECCD component, and full inductive current replacement.

This report will give a brief description of the X2 and X3 systems and relevant diagnostics on TCV in Section 1, followed by a description of the experimental results which have been obtained over the past experimental campaign. These results are divided into two groups: Section 2 will summarize the results of the ECH experiments (zero toroidal launch angle) and Section 3 will describe the ECCD experiments.

1. SYSTEM OVERVIEW:

The TCV tokamak has a vacuum vessel elongation $\kappa=b/a=3$, major radius R=0.89m, minor radius a=0.25m and a maximum vacuum magnetic field of $B_\phi=1.43T$ at the chamber axis. The machine is equipped with 16 independently controlled poloidal field coils allowing the production of plasmas with various elongations (κ_a=1-2.58 achieved), with negative and positive triangularities (δ_a=-0.7 to 1), and at various positions in the vessel. All of these parameters can be changed independently during a shot. This provides a very flexible tool for the study of shaped plasmas.

In view of the wide range of plasma configurations on TCV, a highly flexible auxiliary heating system is required. An ECH system was chosen in light of this requirement owing to its localized heating and steerable beam capabilities. The TCV-ECH system [1] will consist of nine gyrotrons of 0.5MW each. Six gyrotrons will operate at the second harmonic frequency (X2) of 82.7GHz and three at the third harmonic frequency (X3) of 118GHz. The gyrotrons are grouped in clusters of three, with each cluster operating on a single Regulated High Voltage Power Supply (RHVPS) [2].

a) X2 system

Each X2 gyrotron [3] is connected to a matching optics unit (MOU) for optimum coupling into the evacuated corrugated waveguide and absorption of stray radiation from the gyrotron. Incorporated in the MOU is a Universal Polarizer providing the full range of all possible polarizations. Connected to each MOU is an evacuated transmission line (approximately 30m of 63.5mm corrugated HE_{11} waveguide) which includes two DC breaks, in-line bellows, power monitor miter bend, vacuum compatible switch and calorimetric load, in-line pumping-tee and a launching antenna (launcher).

The X2 launcher (shown in Figure 1) is designed to direct the microwave beam at any radial location within the wide range of plasma shapes achievable on the TCV tokamak as shown in Figure 2. For each cluster of X2 gyrotrons there is one launcher mounted in an equatorial port (L1) and two launchers (L2 and L3) mounted in upper lateral ports. Each launcher has 2 degrees of freedom, one of which provides steering of the beam in a fixed plane during a shot (realized by rotating the last mirror), while the other allows that plane to be rotated about the axis of the launcher port between shots. Each gyrotron can be independently switched to the torus or to a calorimetric load from shot to shot, such that power can be delivered from any possible combination of three launchers for a given shot.

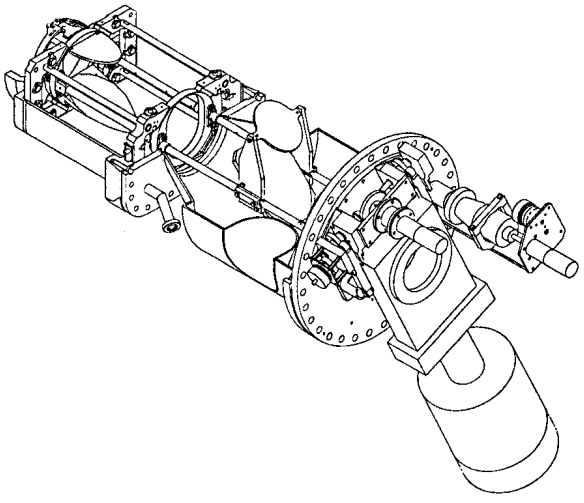

Figure 1. *Drawing of the X2 Launcher with all-metal vacuum gate valve and external motors. The launcher has two degrees of freedom, the beam can be steered within a chosen plane during a shot, and the launcher can be rotated about the port axis between shots to change that plane.*

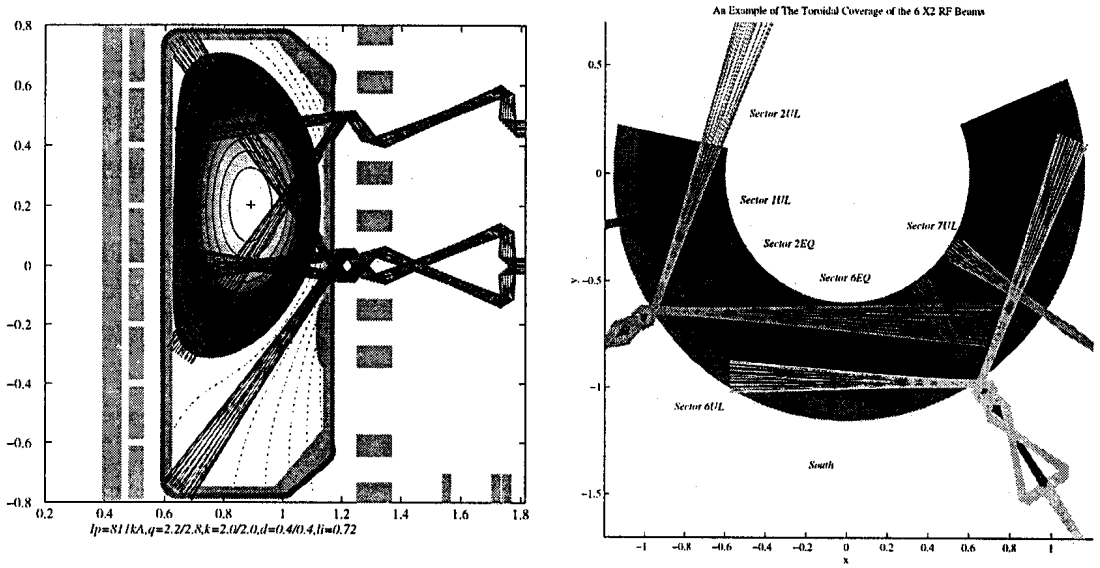

Figure 2. *The accessibility of the X2 launchers in the (a) poloidal and (b) toroidal viewing planes. The 2 launchers of the first cluster gyrotrons are located in upper lateral ports and one in an equitorial port.*

At the present time there is one fully operational X2 cluster on the TCV tokamak. This cluster has had several full power, full pulse length pulses on TCV during the past operational campaign period. All the gyrotrons of the second cluster have passed the acceptance tests and are ready for operation on the tokamak. The associated MOUs and transmission lines are installed and have been vacuum tested. The second cluster launchers are in the process of being installed on the tokamak for operation at the end of 1999.

b) X3 system

Three 0.5MW, 2s gyrotrons [4] at the third harmonic (X3) frequency of 118GHz are planned to be operational on TCV for the end of the year 2000. The X3 gyrotrons will only be operating at pulse lengths of 2.0s even though the full capabilities of the tubes are 210s for use on the Tore Supra tokamak. The first tube has been delivered to CRPP and has successfully passed the on-site acceptance tests, including over 160 pulses of 0.5MW, 2.0s pulses (reliability > 99%) have been obtained with the EC power diverted to a dummy load.

The X3 launcher is mounted on a top port to launch the beam in a direction nearly tangential to the resonant surface thereby maximizing the absorption by increasing the path length through the plasma. The three beams are incident on a single mirror which can be radially displaced (±a/3) between shots to inject the beam from either the low (LFS) or high field side (HFS) of the resonance, see Figure 3. The mirror can also be rotated (±5°) during a shot to adjust the beam along the resonance surface, from any radial location. A prototype of the launcher has been completed and is undergoing mechanical testing. A fully operational launcher is planned to be installed on TCV during the year 2000, thus bringing the full auxiliary heating power available on TCV to 4.5MW before the end of the year 2000.

c) TCV diagnostics

A brief description of some of the more relevant diagnostics used during ECH-ECCD experiments is given below. A more detailed description of these diagnostics can be found in reference [5].

The soft X-ray diagnostic provides the most direct response of the central MHD activity and is comprised of three groups of instruments:

1) four vertically viewing, fast diodes with a sampling rate of 250kHz located in four toroidal positions provide high time resolution of MHD activity.
2) 180 diodes distributed in nine cameras in one poloidal cross section with sampling rate of up to 80kHz and spatial resolution of 3.5cm after tomographic reconstruction.
3) Four additional vertical viewing diodes for measuring the soft X-ray temperature using the two foil method.

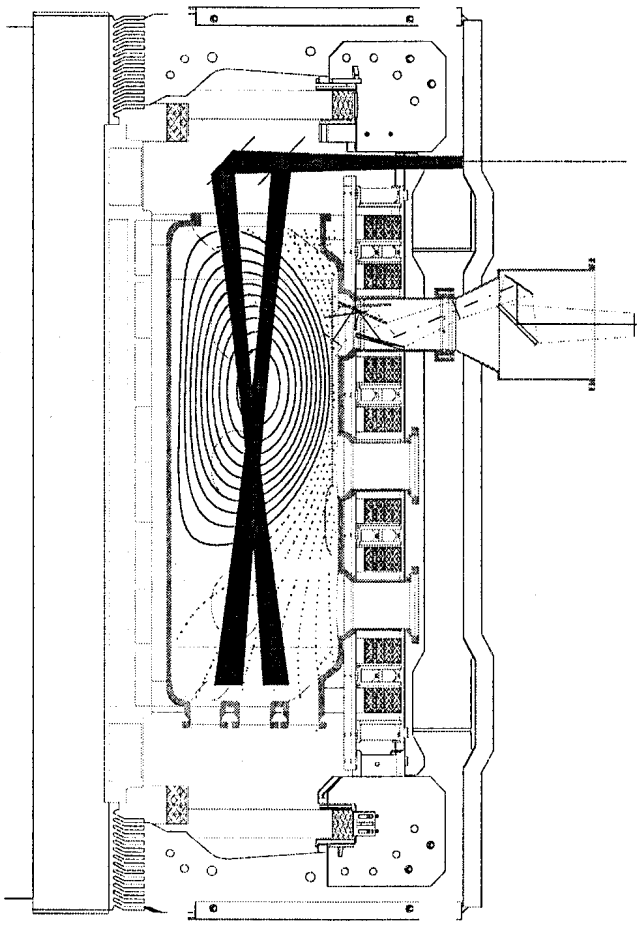

Figure 3. *The X3 Launcher will inject three beams vertically into the plasma. The launcher mirror can be rotated during a shot to change the injected poloidal angle and can be displaced radially between shots.*

The Thomson scattering system on TCV uses three Nd:YAG lasers (each at 20Hz, combined in a fan and focused to a single point in the plasma) aligned in the vertical direction at a single value of the major radius. Thirty-five viewing chords are distributed on three horizontal ports providing a measure of n_e and T_e with a spatial resolution of about 4cm along the laser beam.

A multichannel hard X-ray diagnostic system which characterizes the spectral and spatial distribution of fast electron bremsstrahlung emission has been operational on TCV [6] during part of the operating period. This diagnostic was developed for the Tore Supra tokamak [7] and was on loan to the CRPP from CEA-Cadarache, France. The system provides a spatial resolution of 2.0cm (on the midplane) from 14 viewing chords and an energy resolution of 5-7keV, in the range from 10-150keV.

The LIUQE equilibrium code [8] determines the plasma position and shape from 38 magnetic probes and the plasma pressure profiles from the Thomson scattering system. These results along with the Thomson density and temperature profiles are used by the TORAY [9,10] ray tracing code to compute the beam propagation and absorption location.

2. ECRH EXPERIMENTS

a) X2 Launcher accuracy

A commissioning of each gyrotron/MOU/launcher is performed to ensure that a similar plasma response is observed for each system. The commissioning involves two sets of tests: an alignment test at atmospheric pressure and a plasma response test to ensure optimum coupling to the plasma and the integrity of the launcher alignment under vacuum conditions.

The alignment at atmosphere of each launcher is performed after the installation of each launcher on the torus. The launcher alignment is checked by firing the beam onto a target of liquid crystal paper attached to the vessel's central column. The target is then displaced to two other vertical locations to check the calibration of the movement of the last mirror.

The plasma response test involves the sweeping of each beam across a target plasma ($\bar{n}_e$=1.4-1.9x10^{19}m^{-3}, I_p=173kA, κ=1.3, δ=0.3) as shown in Figure 4. From previous experiments the response on the soft X-ray signal (central chord) was observed to increase/decrease as the beam deposition passed inside/outside the q=1 surface. The soft X-ray signals for the three launchers are shown in Figure 5. The signals for the two upper lateral launchers, L2 and L3, are identical, while the equatorial launcher, L1, is shifted in time due to differences in refraction in launching a beam from an upper lateral or an equatorial port. Large sawteeth are observed over a relatively small region during the sweep when heating near the q=1 surface closest to the launcher despite relatively large beam width (≈30mm) [11]. Comparing the location of these large sawteeth for the two sweeps of L2 and L3 yields a relative measure of alignment of the two launchers which is found to be within ±0.2°(±3mm). L1 can be checked against the results of either L2 or L3 using TORAY. The angle at which these sawteeth occur is compared with the TORAY calculated angle for q=1 deposition. The precision for calculating the q=1 surface is within ±20mm. The TORAY calculated angle and the 'straight' ray angle both fall within the range of the calculated q=1 surface (i.e. refraction is insignificant for the near side q=1).

For both launchers 2 and 3 the realized aiming precision is ±0.2° which is the initial designed restrictions placed on the launcher. Launcher 1 can only be tested relative to the errors associated with the calculations of the q=1 surface from LIUQE and it gives ±1.3° (±20mm). Since the same pre-alignment procedure was performed for all launchers, we have the confidence that launcher 1 has the same order of precision as launcher 2 and 3.

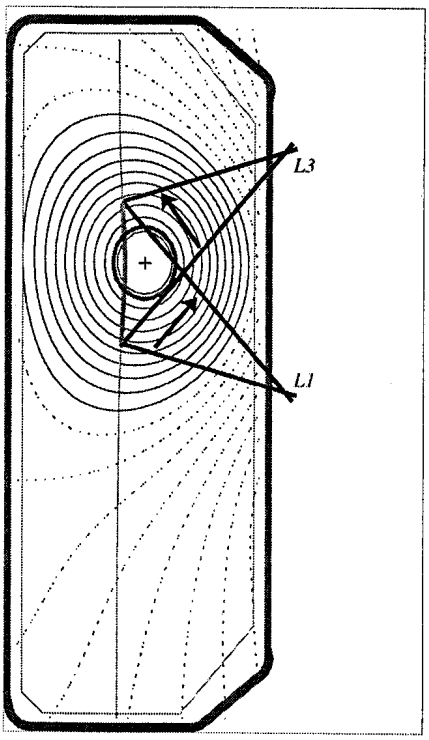

Figure 4. *Swept region of the beam during the commissioning shots. Each launcher is swept from below the q=1 surface to above it.*

b) ECH coupling

Sweeps of the ECH deposition identical to those described above, were performed with non optimal coupling of the beam by changing the X-O mode fraction via the Universal Polarizer located in the MOU. For the X-mode launch the calculated absorbed power is 100% and the coupling changes by less than 5% during the sweep of the beam [11]. The effect of the coupling scan is best seen on the soft X-ray signal as shown in Figure 6. The soft X-ray signal viewed from a central chord increases when the deposition is inside the q=1 surface for X-mode launch. This rise is barely apparent for the O-mode injection.

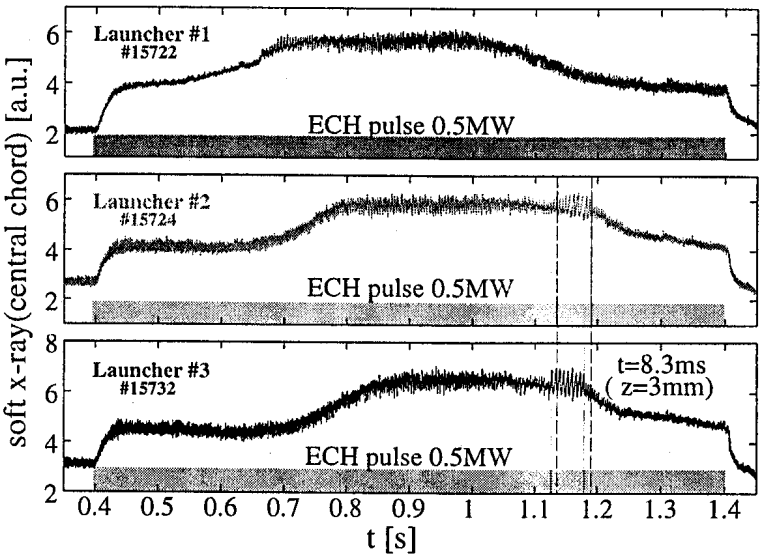

Figure 5. *The soft X-ray response to each launcher sweep as shown from a central chord. The signals of Launchers 2 and 3 are shifted relative to each other by 8.3ms in time, which corresponds to a missalignment of ΔZ=2.9mm in vertical heating location. Launcher 1 is shifted in time owing to a difference in beam refraction between the equatorial and upper lateral ports. The large sawteeth occur on the q=1 side nearest the swept launcher (largest power density).*

As the polarization was varied to increase the X-mode component at the plasma edge, the total stored plasma energy measured by Thomson scattering increased, (see Figure 7). Comparing the plasma's total energy during sweeps at various coupling efficiencies confirms that the optimum heating is obtained within the q=1 surface [5]. For X-mode launch the electron confinement time increases abruptly when deposition is within this region implying the presence of an energy transport barrier near this surface. When absorption occurs within this region the stored electron energy increases by 20% over deposition outside the region. Approximately the same ratio of stored energy is measured between X-mode and O-mode polarization injection cases during central deposition (see Figure 7).

In the poorest coupling case with essentially 100% O-mode coupling little difference is observed when heating inside

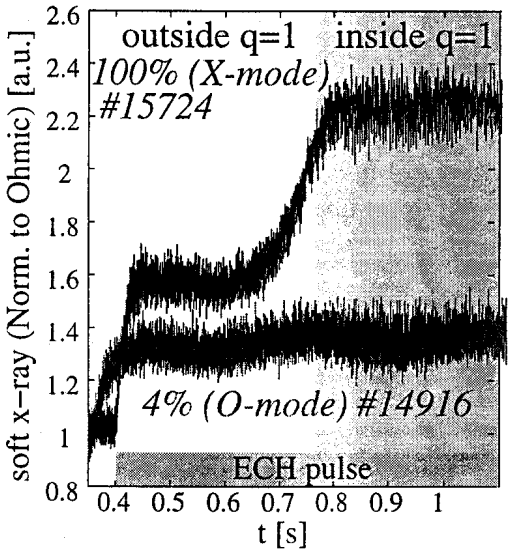

Figure 6. *Difference in a central chord of the soft X-ray signal for two sweeps with X-mode and O-mode coupling respectively. When deposition is inside the q=1 surface the soft X-ray signal increases with X-mode percentage.*

or outside this region. This implies low first pass absorption, with the majority of the beam eventually being either absorbed in the carbon tiles of the tokamak, absorbed in the plasma after multiple reflections, or lost through vacuum windows. The total power absorbed in the plasma is represented by the following:

$$\eta_{eff} = \eta_{fp} + (1 - \eta_{fp})\eta_{mr}$$

where η_{eff} is the percentage of total absorbed power in the plasma, η_{fp} is the percentage of power absorbed on the first pass, and η_{mr} is the percentage of power absorbed after multiple reflections in the torus chamber. The percentage of first pass absorption, η_{fp}, is taken from TORAY calculations. To estimate the percentage of power absorbed after multiple reflections, η_{mr}, the tokamak is modeled as a black box with holes. Radiation incident on a 'hole' escapes the black box. In this case the 'holes' are vacuum windows and the resonant surface. The amount of power 'escaping' (or absorbing) through the resonant surface can be represented by a sum of an infinite series:

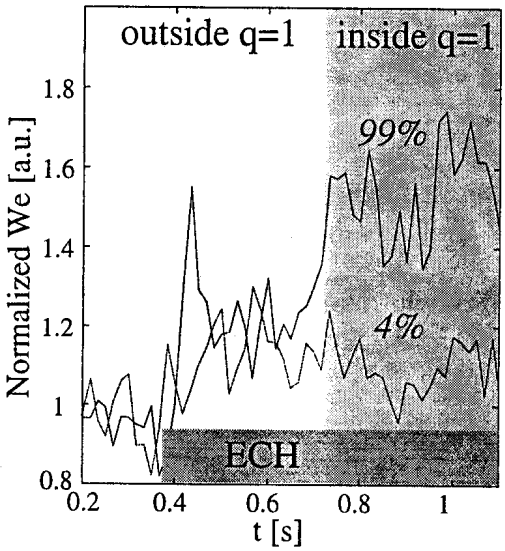

Figure 7. Total stored energy of the plasma for sweeps at various X-mode coupling percentages ranging from 0 to 100%.

$$\eta_{mr} = \frac{R_{wall} \cdot \frac{a_{res}}{A_{total}}}{1 - R_{wall} \cdot \left(1 - \frac{a_{res} + a_{windows}}{A_{total}}\right)}$$

where a_{res} is the area of the absorbing resonant surface (both LFS and HFS), R_{wall} is the average reflection coefficient of the vessel wall, $a_{windows}$ is the sum of the surfaces of the 'holes' or vacuum windows on the torus, and A_{total} is the sum of the areas of a_{res}, $a_{windows}$ and the inside surface of the tokamak. In the case of randomly scattered radiation the beam is assumed to be 50% in X-mode and 50% in O-mode. Full absorption is assumed for X-mode incidence while only 12% for O-mode incidence, based on TORAY calculations for these plasmas. The non-full absorption in O-mode can be compensated by shrinking the size of the absorption surface area based on the average absorption of the two modes, thus the effective area is $0.56 \cdot a_{res}$, an average between the 100% absorption of X-mode and 12% in the case of O-mode.

Applying the above model to the TCV vacuum vessel, assuming a 95% wall reflectance, the absorbed power in the plasma is computed to be 65% of the injected ECH power. Assuming 20% of the absorbed power is inside the q=1 surface (based on ratio of the areas of the resonant surface inside the q=1 versus outside the q=1) from the results of the polarization scan, the total stored energy of the plasma should increase by 24% over the ohmic level. For O-mode injection (shot #14920) the average stored energy increased by 21±7%. This estimation of the

absorbed power is useful for determining the power delivered to the plasma when first pass absorption is low because of coupling, strong refraction in the case of large injection angles, and when density cutoff is exceeded (in the later case, the region of the absorption surface inside the density cutoff region is excluded from the total a_{res}). This model should be valid when $a_{res} << A_{total}$.

c) Confinement studies

Studies of the energy confinement time in ECH discharges have been performed as a function of plasma shape in TCV [12]; to extend previous studies of confinement in Ohmic plasmas [13,14]. Steps of ECH power were used from 0 to 1.5MW which typically represented a power ratio of P_{ECH}/P_{OH} between 0 and 10 during ECH, with the power deposited within the q=1 surface. The shape scans were performed at two different values of the engineering safety factor q_{eng}=1.7 and 3 (q_{eng} = 5abB/RI_p, where $2.3 < q_a < 6$; $0.2 < I_p < 0.7$ MA). A fixed q_{eng} implies a nearly constant normalized radius of the q = 1 surface while changing the plasma shape based on analysis of the ohmic database [15]. The stored electron energy is measured during stationary periods from repetitive Thomson scattering measurements (60 Hz), typically averaged over 10 time-slices.

A general power scaling law has been obtained over the full data set describing the dependence of the electron energy confinement time τ_{Ee} (ms) on the average line density $\bar{n}_e$ (10^{-19}m^{-3}), total power P (MW), edge elongation κ, edge triangularity δ, and plasma current I_p (kA) using a multi-variable regression fit. The dependences on κ and I_p cannot be separately determined, owing to the strong correlation between these quantities in the present data base. The power law must therefore contain a free parameter, and takes the following form [12]:

$$\tau_{Ee}[ms] = 2 n_e^{\alpha_n} P^{\alpha_P} (6 I_P)^{\alpha_I} \kappa^{\alpha_\kappa} (1+\delta)^{\alpha_\delta}$$

with α_n=0.46±0.2, α_P=-0.7±0.1, α_δ=-0.35±0.3, α_κ=1.4(1-α_I)±0.4, where α_I remains undetermined. The uncertainties have been estimated assuming a 25% error on τ_{Ee}. Good fits are obtained with α_I in the range $0 \le \alpha_I \le 0.7$, an example at α_I=0.5 is shown in Figure 8.

In spite of the unresolved confinement dependence on current and elongation, the trend toward increasing elongation for improved confinement is present. The main motivation for creating elongated discharges is indeed to increase the plasma current with the aim of increasing the energy confinement and pressure limits.

Further experiments are needed to separate the contributions of plasma current

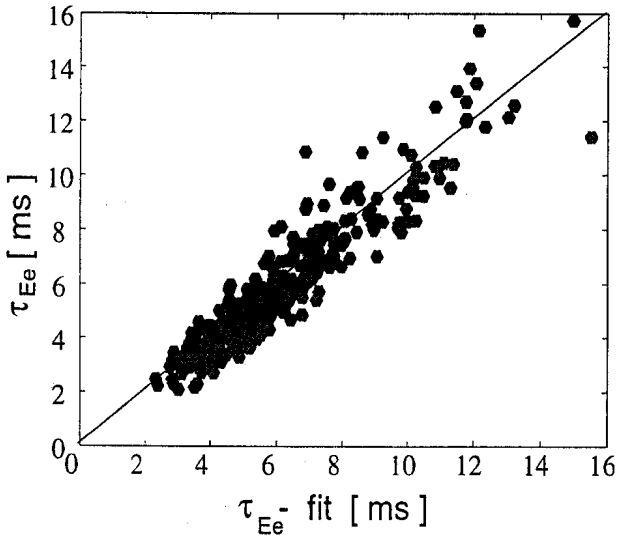

Figure 8. Empirical scaling law for TCV ECRH data set, in the representative case α_I=0.5 [12].

and elongation. Higher ECH power levels will be possible when the second cluster becomes available so that the ratio of additional power to the total power can be large even at high plasma current.

The general scaling obtained above can be compared with the recent scaling laws found using a multi-tokamak database, such as the ITER-98-L mode scaling, where α_n=0.40, α_P=-0.73, α_I=0.96, α_κ=0.64 [16], as shown in Figure 9. Within the uncertainties, the exponents, α_n and α_P found in TCV are in agreement with those of the ITER-98-L scaling; however, α_κ and α_I are not both compatible with the ITER-98-L scaling.

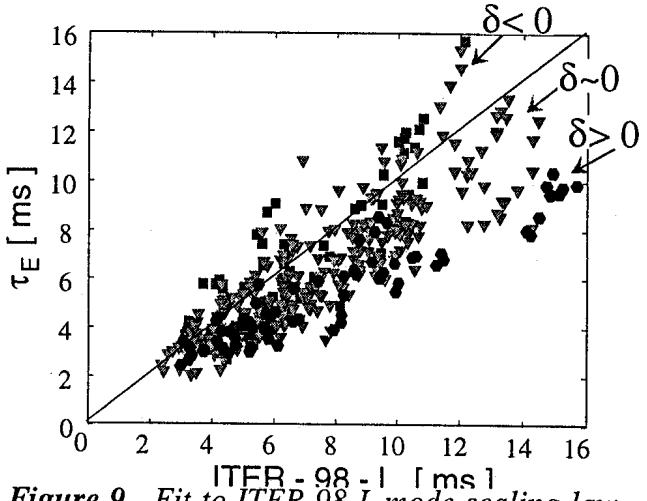

Figure 9. *Fit to ITER-98-L mode scaling law. Since triangularity does not appear in ITER-98-L, it is explicitly indicated by the symbols: negative δ appear favourable (red squares: δ<0, green triangles: 0<δ<0.3, blue hexagons: δ>0.3) [12].*

An improvement in confinement with negative triangularities is responsible for the spread in the comparison with the ITER-98-L modes scaling (ITER-98-L does not include a triangularity dependence). The improvement, however, becomes less pronounced at higher powers (lower τ_e on Figure 9).

d) L-H mode transition

Ohmic H-mode plasmas are regularly obtained in TCV (limited or diverted, single or double null, $3<\bar{n}_e<9\times10^{19}$ m^{-3}, $1.1\leq B\leq1.5$T, $1.05\leq\kappa\leq2.05$, $-0.2\leq\delta\leq0.7$, $2.05\leq q_{95}\leq4$). Since L-H transitions are rarely observed in low density plasmas ($\bar{n}_e\leq4\times10^{19}$ m^{-3}), the goal of this experiment was to find out if H-mode could be accessible with a low density ECH target plasma.

Central deposition with 1.5MW tends to result in a disruption. This was avoided by spreading out the deposition region along the plasma minor radius(vertically).

The low density limit of H-mode accessibility was lowered with the addition of ECH power[17]. An example of such a discharge is shown in Figure 10. The transitions were obtained in 3 successive ramps of the ECH power. The occurrence of the L-H transition varied with ECH power depending on the plasma parameters. The absorbed ECH power was calculated from the sum of first pass absorption from TORAY and multi-pass absorption from the modified black-box model described previously.

A clear demonstration of the improved range of H-mode accessibility is shown in Figure 11: whereas, previous Ω-H transitions were limited to line average densities above 3.5×10^{19}m^{-3}, the density threshold is lowered by 28% to 2.5×10^{19}m^{-3} with the addition of the ECH power. Within this extended regime the power required to initiate a transition increases with decreasing density in contradiction of ITER power scaling laws [16]. This inverse dependence was also observed on COMPASS in ECH assisted L-H transition [18]. These independent observations tend to confirm the discrepancy between heating schemes acting on ions and those acting

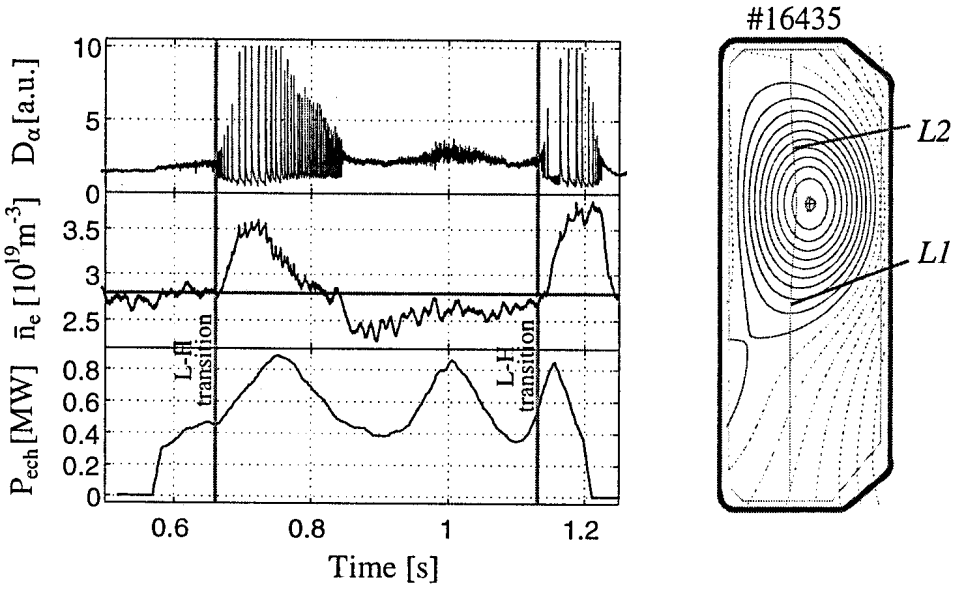

Figure 10. Time evolution of a discharge with L-H transition induced by ECH. The Two L-H transitions which occur during this particular discharge are identified by the vertical lines. The plasma poloidal cross section at the time of the first L-H transition is shown at right [17].

on electrons in terms of H mode accessibility.

The limited data base of L-H transitions showed no noticeable change of $P_{Thresh-old}$ with the plasma shaping.

3. ECCD EXPERIMENTS

a) Toroidal Launch Angle Scan

A scan of the launcher's toroidal injection angle has been performed over a range from -35° (counter-ECCD) to +40° (co-ECCD) with ECH power of 1.5MW ($\bar{n}_e$=1.4-1.9x10^{19}m^{-3}, I_p=173kA, κ=1.3, δ=0.3). At each toroidal angle the plasma was displaced in vertical position during the shot so that there were two periods of on-axis deposition and one intermediate period of off-axis. Typically, the on-axis heating produced centrally peaked T_e profiles throughout the scan while off-axis heating yielded broader profiles with lower central temperatures as shown in Figure 12 [19]. The highest central electron tempera-

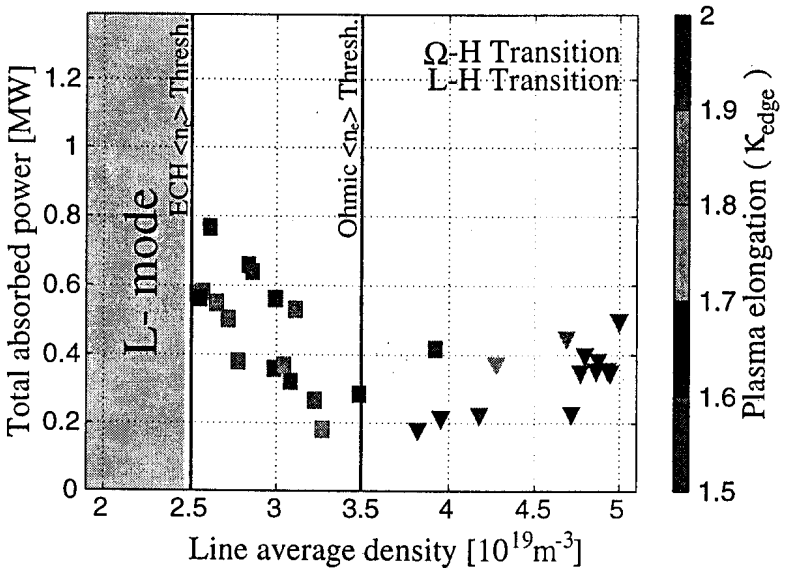

Figure 11. L-H transition threshold power in ohmic (triangles) and ECH (squares) plasmas [17].

tures of ~10keV were achieved with counter-ECCD at -14°.

The product of the loop voltage and the volume average of the $Te^{3/2}$ dependency on the toroidal injection angle is plotted in Figure 13 for on-axis deposition. During co-ECCD V_s continues to decrease with increasing injection angle. This differs from initial calculations which predicted optimization of the co-ECCD between 25 and 30° using non-linear Fokker-Planck calculations [20]. At large toroidal angles the beam undergoes strong refraction and first pass absorption becomes less than 100%, TORAY results calculate ≈70% for the case of ϕ=35° at these densities. Since the electron temperature is lower off axis, the driven current can be expected to decrease as the deposition moves off-axis. This was seen in the difference of the loop voltage between the on- and off-axis heating phases of the discharge. The results of this scan imply that the optimum current drive occurs at larger than predicted toroidal angles, $\phi \geq 35°$.

The spectral distribution of the fast-electron bremsstrahlung emission was measured during the scan of the toroidal angle by the multichannel hard X-ray diagnostic system on loan from CEA, France [7]. The photon counts from the bremsstrahlung emission increased at all energy levels as the toroidal angle increased in both the co- and counter- directions, see Figure 13. The results from the spectral distribution during the launch at ϕ=0° were Maxwellian and agreed with the electron temperatures measured by Thomson scattering. As a non-zero toroidal

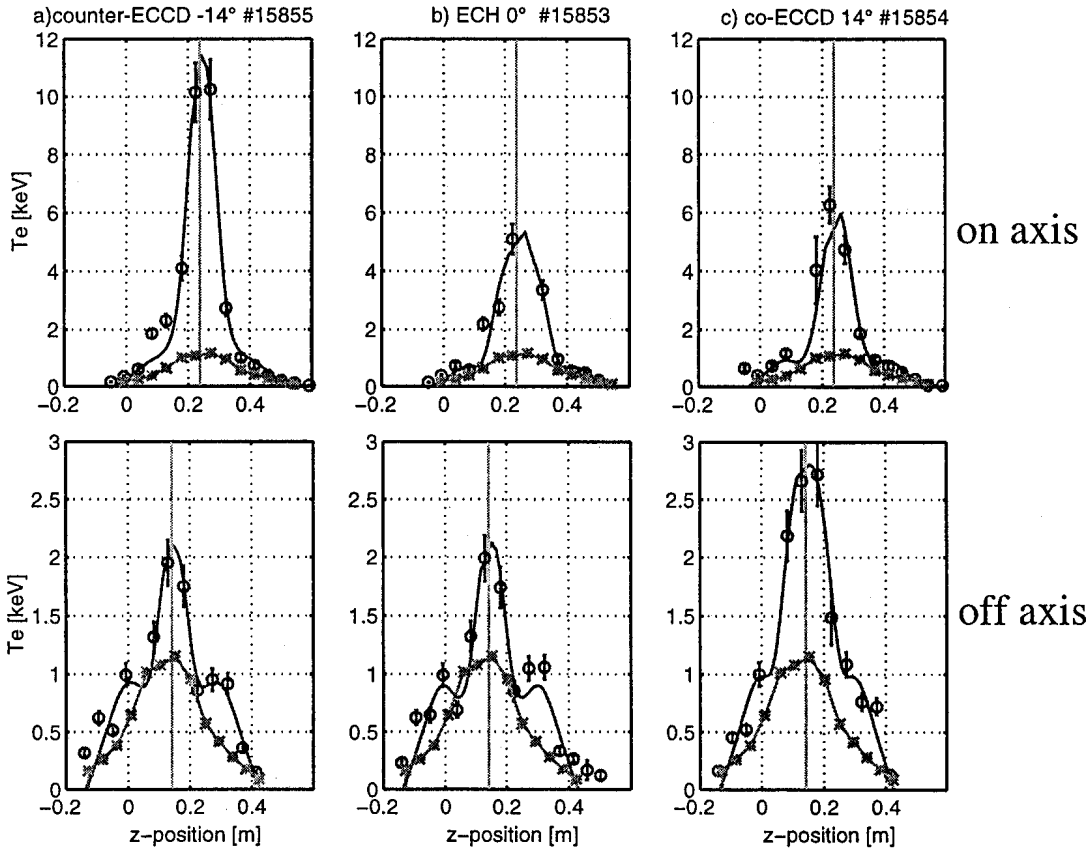

Figure 12. *Electron temperature profiles from Thomson scattering for on- and off-axis ECCD and ECH discharges. Highest observed temperatures (10keV) have occured at -14° counter-ECCD. On-axis heating yields centrally peaked profiles while off-axis heating results in broader, lower temperature profiles [19].*

angle was introduced, a non-Maxwellian suprathermal tail developed [6]. This is consistent with theoretical expectations for ECH and ECCD discharges. During ECH, the lowest energy electrons are in resonance with the full power of the beam: attenuation of the beam leads to less power being available to heat the higher energy electrons. During ECCD, conversely, the higher energy electrons are in resonance first. With a non-zero toroidal angle the beam preferentially heats electrons on the low field side of the cold resonance which have a finite parallel velocity, due to the Doppler-shift. This results in the generation of a suprathermal tail in the electron velocity distribution.

b) Up-Down Asymmetry

An up-down asymmetry has been observed during launcher sweeps similar to those shown in Figure 4 [21]. This asymmetry is most pronounced in the behavior of the sawtooth shape and period when the deposition is near the q=1 surface. Even though the sweep of the beam was kept in a poloidal plane (no toroidal injection angle), the asymmetry has been shown to be a result of a small current drive component arising from the non-zero projection of the wave vector **k** on the magnetic field for off-axis heating - thereby producing Doppler-shifted absorption. This is portrayed in Figure 14. The direction (co/counter) and magnitude of ECCD will depend on the absorption location, launch direction (HFS versus LFS) and toroidal field direction but not on the plasma current direction. The poloidal field and the plasma current producing it have the same sign: therefore simply reversing the plasma current will not change the relative direction of the ECCD (e.g. co-ECCD will remain co-ECCD). Because it is the poloidal field that creates the asymmetry, the effects are seen only during off-axis absorption. This effect is confirmed by TORAY calculations which show linear current drive efficiencies changing sign when heating below or above the plasma midplane. The ECCD direction can be reversed by reversing B_ϕ [11].

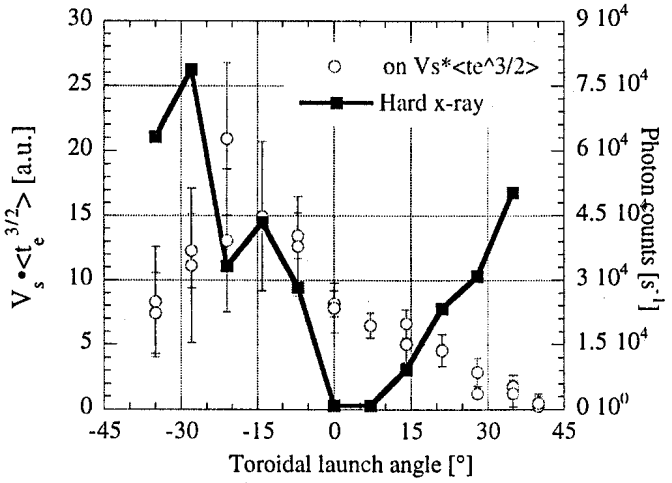

Figure 13. *Plasma loop voltage for on-axis deposition and photon counts (between 40-50keV, on axis deposition)[6] dependence on the toroidal launch angle.*

Initial ECCD experiments on TCV showed a change in the behavior of the sawteeth shape (co- produced large triangular sawteeth, counter- produced humpbacks) and period between co- and counter- ECCD which occurs even at low ECCD efficiencies at equivalent levels as calculated by TORAY for the off-axis ECH case described above.

Numerous effects of sweeping the deposition across the q=1 surface are seen; these include: a) density pump-out, b) rise in central temperature, c) increase in line-integrated X-ray emission (as viewed from central chords), d) the sawtooth period and amplitude increase at the transition from outside to inside, e) the width of the transition region is larger when passing from inside to outside (rather than outside to inside), f) the amplitude of the peak in sawtooth period increases with co-ECCD and decreases with counter-ECCD (produced by intentionally

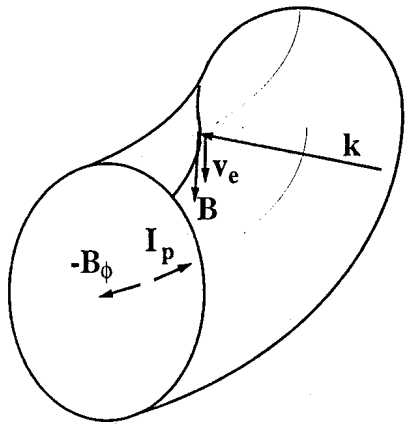

*Figure 14. Sketch of **k** and **B** vectors with off-axis deposition. There is an inherent ECCD component due to a non-zero projection of **k** onto **B** arising from the poloidal magnetic field (v_e is the electron velocity vector).*

introducing small toroidal angles).

The q=1 transition region is of particular interest because it allows the confirmation that ECCD is responsible for the non-axisymmetric plasma response. Large roughly triangular sawteeth appear only when heating near the upper q=1 surface with the upper lateral launcher (L3) and not with the equatorial launcher (L1). Non-triangular, but nevertheless large, sawteeth occur when heating near the lower q=1 surface with L1 and not L3. When B_ϕ is reversed, these results are reversed as well, with L1 playing the role of L3 and vice versa. This leads to the conclusion that the sawtooth shape strongly depends on the driven current direction [11] when the deposition is on or near the q=1.

In another experiment, the beam deposition on the transition region was kept constant while the beam power was increased, thus varying the power density. Resulting sawteeth do not change shape but become larger with power density. The period increases linearly with power. The large sawteeth can be eliminated or enhanced with the intentional addition of a toroidal angle of the launched beam. The resulting peaks in sawtooth period as well as the sawtooth shapes are shown in Figure 15. Positive angles decrease (with reversed B_ϕ) the ECCD component: +4° corresponds to pure ECH. Large triangular sawteeth only occur with a co-ECCD component and when the absorption occurs over a narrow extent in minor radius. Similarly, large triangular sawteeth can be created by over-compensating the inherent counter-ECCD offset leading to co-ECCD. The narrow range in which the large sawteeth occur allows the determination of the beam absorption region as was performed for the alignment tests mentioned previously. If the location of the large sawteeth can be proven to be a physical relevant location of interest, such as the q=1 surface, it could provide a useful tool for testing models describing the sawtooth instability. Tokamaks with ECH but not equipped to measure the q-profile could then find this location by sweeping the heating location and constrain equilibrium reconstruction codes accordingly.

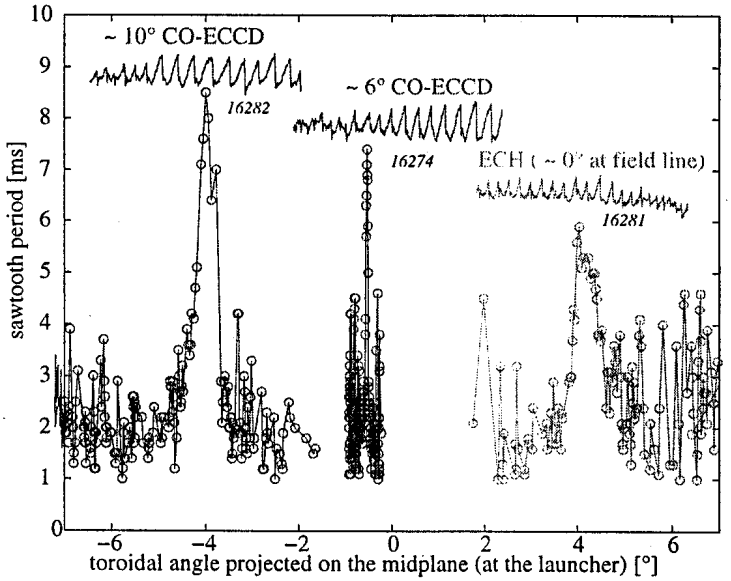

Figure 15. The sawtooth period about the q=1 surface with the launching plane rotated ±8° about the poloidal plane. The co-ECCD component has been eliminated on the q=1 surface with the introduction of a counter-ECCD toroidal angle (#16281) [11].

c) Full current replacement with ECCD

The principal aim of this experiment was to obtain a fully non-inductive stationary scenario using three 0.5MW gyrotrons [22]. From previous experiments of scanning the toroidal launch angle the optimum toroidal angle was found to be ≥35°. For this study a toroidal injection angle of 35° was chosen. The deposition profile to maximize the sustainable driven plasma current.

To obtain the maximum driven current the three launchers were aimed at near central deposition where highest efficiency occurs owing to highest temperatures. It was possible to obtain 153kA of fully non-inductive current for 150ms (n_{e0}=2.0·$10^{19}$$m^{-3}$, T_{e0}=4.5keV), before the discharge disrupted. The width of the power deposition was small (10-20% of minor radius) resulting in peaked current and temperature profiles. MHD modes became unstable and caused the disruption. Neoclassical tearing modes were also destabilized and degraded the performance of the discharge. To avoid these modes the power deposition of the three gyrotrons was then spread out over the minor radius such that the overall power deposition profile resembled the current density profile, as shown in Figure 16, with ρ=0., 0.3, 0.55. This results in a lower central temperature (T_{e0}=3.5keV) and smaller driven current (I_p=123kA) but achieved a stable fully non-inductive current for 1.9s (n_{e0}=1.5x10^{19} m^{-3}), see Figure 17. The current in the ohmic transformer was held constant which is the most sensitive measurement of full current replacement. The loop voltage quickly decreased to zero at the turn on of ECCD, while the equilibrium profile (κ and l_i) evolved over 0.5s. Once the profile reached equilibrium the discharge was maintained for 1.4s, approximately three times the period for achieving equilibrium.

The shots were repeated with I_p=112kA and 127kA to demonstrate the exact control of the driven current. In the first scenario the transformer was charging up during the discharge implying the current was driven in excess while in the second case the transformer discharged implying insufficient current replacement. The current drive efficiency is consistent for the

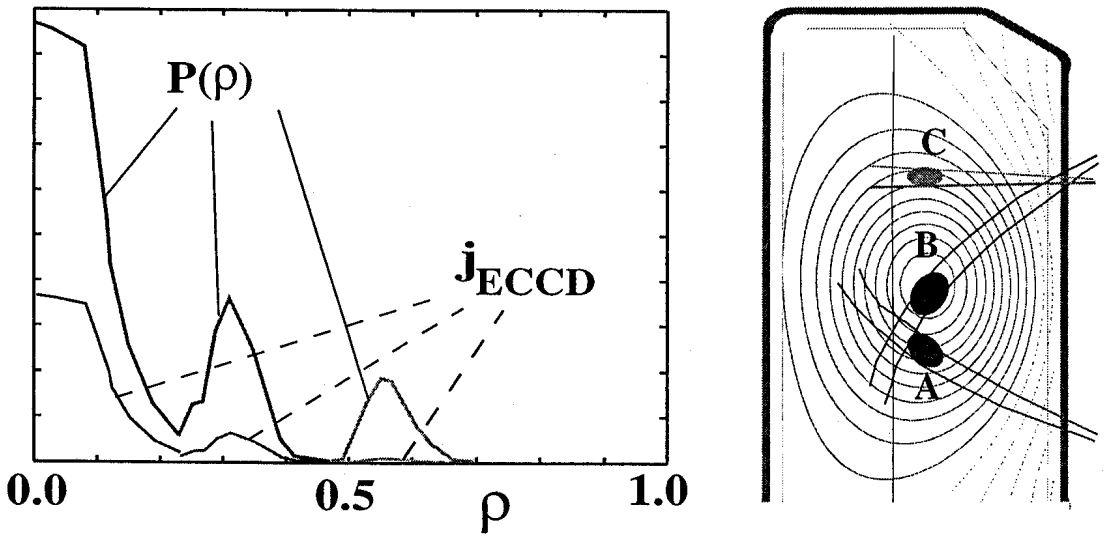

Figure 16. The power and current density profiles from Toray for the fully non-inductive current replaced discharge. The deposition of the beam projected in a poloidal plane is depicted at right [22].

three shots (taking into account the change in density between shots) at I_p=123kA and I_p-I_{CD}=11kA for $|V_s|$=0.02V. TORAY calculations are in agreement with a driven current of 120kA (η_{ECCD}=0.08A/W). The peaked profile of these discharges leads to a non-negligible bootstrap current of 25kA as calculated in reference [23]. Taking the bootstrap current into account TORAY overestimates the driven current by about 20%, which is within the error bars of the injected power and the density and temperature profiles used in the calculation.

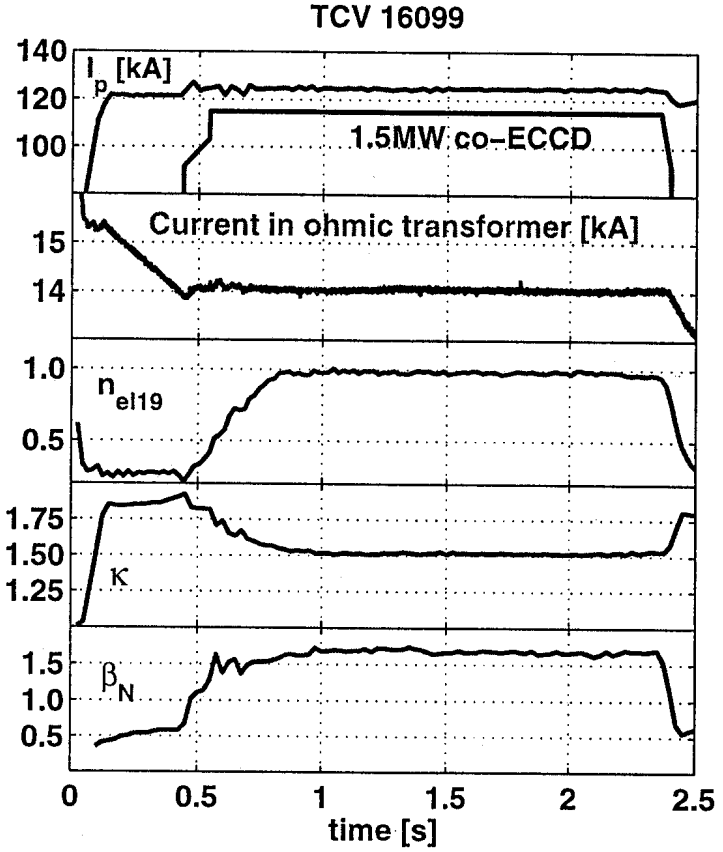

Figure 17. Steady-state fully non-inductive discharge for 1.9s using 1.5MW of co-ECCD with the power distribution depicted in Figure 16. Note that the equilibrium profiles require 0.5s to settle. [22]

As previously stated, the amount of current driven decreases as the beam is moved off axis. The amount of driven current from the beam 'C' (Figure 16) is calculated from TORAY as 2.5kA, near ρ=0.55. This beam is important for broadening the pressure and, possibly, the current profile: this is tested by keeping the deposition location the same but removing the toroidal injection angle (ECH rather than co-ECCD). The feedback plasma current is then decreased until V_s=0. The difference in plasma current is 7-9kA which confirms the results obtained on DIII-D [24] that more current can be driven off-axis than predicted.

SUMMARY

The first 1.5MW of the ECH system on TCV has been operated with up to 2.0s pulse lengths during the latest operational campaign. The second 1.5MW of ECH power (X2) is planned to be operational by the end of the current year bringing the total auxiliary power available in TCV to 3.0MW. The X3 system implementation is progressing with the delivery and successful acceptance of the first gyrotron. A preliminary design of the X3 launcher has been made and is under test. First planned operation with the X3 system should occur by the end of the following year.

A variety of experimental programs have been performed during this period. During the ECH related studies: the launching antenna system alignment on TCV has been measured to be accurate to within ±3mm during a poloidal sweep; the dependence of the confinement has been

shown to favor increased elongation and negative triangularities; and successful L-H transitions have occurred below the previous ohmic H-mode density threshold ($3.5x10^{19}m^{-3}$), down to a density of $2.5x10^{19}m^{-3}$.

Results of the ECCD experiments include: demonstration that the observed up-down asymmetry is due to an inherent ECCD component when heating off-axis in a nominally ECH scenario; highest TCV central electron temperatures of ≈10keV have been achieved with -14° counter-ECCD; the presence of a non-Maxwellian suprathermal electron tail during ECCD has been measured with the hard X-ray diagnostic system, consistent with preferentially heating electrons at a Doppler-shifted resonance on the LFS; for maximum driven current the optimum toroidal injection angle is ≥35°, higher than initial predicted range of 25-30°; and full non-inductive current replacement of 123 kA for 1.9s has been achieved. The discharge was sustained for over 400•τ_e and four current diffusion times.

ACKNOWLEDGEMENTS:

This work was partially supported by Swiss National Science Foundation.

REFERENCES

[1] T.P. Goodman et al., Proc. 19th SOFT, Lisbon vol. 1 (1996) 565.
[2] G. Besson et al., SOFT 1994, vol. 1, p.517-520.
[3] Bogdanov et al., Strong Microwaves in Plasmas 1993, vol. 2, p.830-835.
[4] C. Tran et al., Proc. of 23rd Int. Conf. on Infrared and Millimeter Waves, Colchester, UK, (1998) edited by T.J. Parker and S.R.P. Smith, ISBN 0 9533839 0 3.
[5] Z.A. Pietrzyk et al., Nuclear Fusion **39** (1999) 587.
[6] S. Coda et al., Proc. of 26th EPS Conf. on Contr. Fusion and Plasma Physics, Maastricht, 1999.
[7] Y. Peysson and R. Arslanbekov, Nucl. Instr. and Methods, **380** (1996) 423.
[8] F. Hofmann and G. Tonetti, Nucl. Fusion **28** (1988) 1871.
[9] K. Matsuda, IEEE Trans. Plasma Sci. **17** (1989) 6.
[10] R.C. Meyer et al., Nucl. Fusion **29** (1989) 2155.
[11] T.P Goodman et al., Proc. of 26th EPS Conf. on Contr. Fusion and Plasma Physics, Maastricht, 1999.
[12] A. Pochelon et al., 17th IAEA Fusion Energy Conf. 1999, CN-69/EX8/3, to appear in Nuclear Fusion, Yokohama Special Issue (1999).
[13] J-M. Moret et al., Phys. Rev. Lett. **79** (1997) 2057.
[14] H. Weisen et al., Nucl. Fusion **37** (1997) 1741.
[15] H. Weisen et al., Plasma Phys. Control. Fusion **40** (1998) 1803.
[16] K. Thomsen et al., 17th IAEA Fusion Energy Conf. 1998, CN-69/ITER/3-ITERP1/97.
[17] Y. Martin et al., Proc. of 26th EPS Conf. on Contr. Fusion and Plasma Physics, Maastricht, 1999.
[18] A.W. Morris, IAEA 1998, CN-69/EXP2/04.
[19] R. Behn et al., Proc. of 26th EPS Conf. on Contr. Fusion and Plasma Physics, Maastricht, 1999.
[20] A. Pochelon et al., Bull. Am. Phys. Soc. **41** (1996) 1514.
[21] T.P. Goodman et al., Proc. of Joint ICPP 1998 and 25th EPS Conf. on Contr. Fusion and Plasma Physics, Praha 1998, ECA **22C** (1998) 1324.
[22] O. Sauter et al., Proc. of 26th EPS Conf. on Contr. Fusion and Plasma Physics, Maastricht, 1999.
[23] O. Sauter et al., to appear in Phys. Plasmas, July (1999).
[24] T.C. Luce et al., General Atomics Report (1999) GA-A23018.